IEICE TRANS. COMMUN., VOL.E90–B, NO.3 MARCH 2007

PAPER

A Fast Algorithm for 3-Dimensional Imaging with UWB Pulse Radar Systems

Takuya SAKAMOTO[†a)], ***Member***

SUMMARY Ultra-wideband pulse radars are promising candidates for 3-dimensional environment measurements by autonomous robots. Estimating 3-dimensional target shapes by scanning with an omni-directional antenna is an ill-posed inverse problem. Conventional algorithms such as the synthetic aperture method or parametric algorithms have a problem in terms of their calculation times. We have clarified the existence of a reversible transform between received data and target shapes for 3-dimensional systems. Calculation times are remarkably reduced by applying this transform because it directly estimates target shapes without iterations. We propose a new algorithm based on the transform and present an application example using numerical simulations. We confirm that the proposed algorithm has sufficient accuracy and a short calculation time.

key words: *3-D, imaging, ultra-wideband (UWB), pulse radar, fast algorithm*

1. Introduction

Three dimensional environment measurement is an important issue for various applications including rescue robots. Ultra-wideband (UWB) pulse radar systems have an advantage that they work even in critical situations where optical measurement is not possible. Estimating target shapes in the near-field using received radar data is an ill-posed inverse problem; many kinds of imaging algorithms have been proposed for this type of problem.

A synthetic aperture algorithm is such proposal, and is often used for geographical imaging from airplanes and satellites [1]. This technique can also be used for near-field imaging with UWB pulse radars. One such system is a GPR (Ground Penetration Radar), such as are utilized for detection of embedded pipes or anti-personnel mines [2]. Bond et al. [3] applied this technique in a UWB pulse radar system for early detection of breast cancer. Narayanan et al. [4] studied synthetic aperture imaging with a through-wall imaging experiment, in which targets behind a wall were reconstructed. These synthetic aperture algorithms utilized Green's function without information of polarization. Kruk et al. [5] proposed a synthetic aperture algorithm of vector waves for a GPR by utilizing the polarization. Synthetic aperture imaging has the advantage of stability, which enables it to be applied in the various applications noted above. However, synthetic aperture imaging requires long calculation times because of its repetition procedures.

Manuscript received July 19, 2006.
Manuscript revised October 4, 2006.

[†]The author is with the Department of Communications and Computer Engineering, Graduate School of Informatics, Kyoto University, Kyoto-shi, 606-8501 Japan.
a) E-mail: t-sakamo@i.kyoto-u.ac.jp

DOI: 10.1093/ietcom/e90–b.3.636

Other kinds of algorithms have also been studied. Migration algorithms are often used for imaging in seismic prospecting [6]. Leuschen and Plumb [7] applied a migration algorithm for GPR with the FDTD (Finite Difference Time Domain) method. However, it is necessary to calculate backward wave equations many times for all grids, which makes it difficult to apply these algorithms to real-time operations. The model fitting method is another approach to this problem [8]–[14]. In the model fitting method, target shapes are expressed with parameters, and these parameters are updated to minimize differences between observed and the estimated data. The model fitting method works well to some extent, but it also has the problem of a long calculation time [15], [16]. Imaging algorithms based on the domain integral equation are another parametric approach [17]–[23]. In their algorithms, targets and media were modeled as grids of permittivity. They solved the domain integral equation with various optimization algorithms, which needed long computation times because of the many unknown variables needing to be solved. Diffraction tomography is also known as an algorithm for non-destructive investigations [24]–[28]. This technique gives an image by deterministic processing in the wave number region. However, it requires a lot of antennas surrounding the target, which strongly restricts its applications.

In general, conventional radar imaging algorithms require long calculation times, a large obstacle for their application to real-time situations such as for use in robots. To overcome this problem, we have proposed a high-speed 2-D imaging algorithm, the SEABED algorithm [29]–[32]. This algorithm is based on boundary scattering transform (BST), a reversible transform and one that can be used for direct estimations of target shapes. In this paper, we show that this transform can be easily extended from 2-dimensions to 3-dimensions. Calculation times are considerably reduced compared to conventional algorithms. We propose a high-speed 3-dimensional imaging algorithm and demonstrate its application examples. In addition, we compare the proposed algorithm with a synthetic aperture algorithm, a conventional algorithm.

2. System Model

In this paper, we assume a monostatic radar system. An omni-directional antenna is scanned on a plane as in Fig. 1. Pulses are transmitted at a fixed interval and received by the same antenna. The received data is input into an A/D

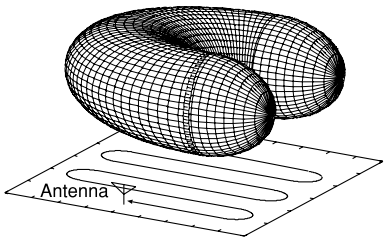

Fig. 1 System model and antenna scanning.

converter and stored in a memory. We then estimate target shapes using the data. We assume that the data is without noise. The transmitted pulse is a mono-cycle pulse without DC power.

We deal with a 3-dimensional problem. We define a real space as the space expressed with the parameters (x, y, z), where targets and the antenna are located. All of x, y and z are normalized by λ, which is the center wavelength of the transmitted pulse in vacuum. We assume $z > 0$ for simplicity. The antenna is scanned on the x-y plane in the real space. UWB pulses are transmitted from the antenna with linear polarization. We define $s'(X, Y, Z)$ as the electric field received at the antenna location $(x, y, z) = (X, Y, 0)$, where we define Z with time t and the speed of the radiowave c as $Z = ct/(2\lambda)$. It should be noted that the received data is expressed with (X, Y, Z), and target shapes are expressed with (x, y, z). The transform from (X, Y, Z) to (x, y, z) corresponds to the imaging we deal with in this paper. We apply a matched filter of the transmitted waveform to $s'(X, Y, Z)$. We define $s(X, Y, Z)$ as the output of the filter. We define a data space as the space expressed by (X, Y, Z). We normalize X and Y by λ and Z by the center period of the transmitted waveform, respectively.

3. Boundary Scattering Transform and Its Inverse Transform

3.1 Boundary Scattering Transform

In this and the following sections, we show that a reversible transform exists between received data and the target boundary surfaces. The reversible transform, BST (Boundary Scattering Transform) was originally defined for 2-D imaging [29]–[32]. We assume that each target has uniform permittivity, and is surrounded by a clear boundary. This assumption is valid for most artificial targets in environments relevant to household or rescue robots. First, we explain the conventional BST for 2-D systems. The upper figure in Fig. 2 shows an example of a target boundary. The symbol of the antenna in this figure shows the position of the omnidirectional antenna that is used as both the transmitting and receiving antenna. A strong echo is received from point "A" on the boundary due to the perpendicular condition. The relationship between X, the position of the antenna, and Z the delay time is shown in the lower figure in Fig. 2. This curve is called a quasi wavefront, and is extracted from received

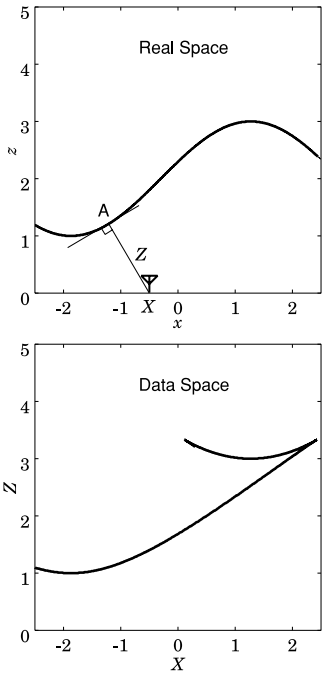

Fig. 2 Example of a boundary scattering transform.

signals. Z of a quasi wavefront is the delay time of the scattered signal, which is easily measured by a UWB radar system. The position of the antenna X is also easy to obtain. The transform from a point (x, z) on the target boundary and a point (X, Z) on the quasi wavefront is expressed as

$$\begin{cases} X &= x + z\mathrm{d}z/\mathrm{d}x \\ Z &= z\sqrt{1 + (\mathrm{d}z/\mathrm{d}x)^2}. \end{cases} \tag{1}$$

Equation (1) is 2-D BST (Boundary Scattering Transform). We have already shown that this transform has its inverse transform, which can be used for fast imaging because (x, z) is nothing but a target shape.

Next, we derive a 3-D BST, which is indispensable for fast 3-D imaging. The normal vector of a target boundary at (x, y, z) is parallel to $[\partial z/\partial x, \partial z/\partial y, -1]^{\mathrm{T}}$. The ray path perpendicularly reflected at (x, y, z) is on the straight line expressed with a parameter u as

$$\begin{bmatrix} X \\ Y \\ 0 \end{bmatrix} = \begin{bmatrix} x \\ y \\ z \end{bmatrix} + u \begin{bmatrix} \partial z/\partial x \\ \partial z/\partial y \\ -1 \end{bmatrix}. \tag{2}$$

It is easily determined that $u = z$ because of the 3rd element in Eq. (2). X, Y and Z are expressed as

$$\begin{cases} X &= x + z\partial z/\partial x \\ Y &= y + z\partial z/\partial y \\ Z &= z\sqrt{1 + (\partial z/\partial x)^2 + (\partial z/\partial y)^2}, \end{cases} \tag{3}$$

where (x, y, z) is a point on a target boundary, and we assume $z > 0$. We define the transform in Eq. (3) as 3-D BST (Boundary Scattering Transform) or as just BST in this paper. This 3-D BST can be interpreted as a transform obtained by generalizing the 2-D BST because if we substitute $\partial z/\partial y = 0$ to Eq. (3), we obtain the 2-D BST.

3.2 Inverse Boundary Scattering Transform

We show the inverse transform of a 3-D BST. The inverse transform of a 2-D BST is written as [29]

$$\begin{cases} x &= X - Z\mathrm{d}Z/\mathrm{d}X \\ z &= Z\sqrt{1-(\mathrm{d}Z/\mathrm{d}X)^2}. \end{cases} \tag{4}$$

The 3-D IBST, which is the inverse transform of the 3-D BST, is obtained in the similar way as in the 2-dimensional case [29]. IBST is based on a back projection process. If there is a reflection at (X, Y, Z) in the data space, the target is on a sphere with its center $(X, Y, 0)$ and its radius of Z in the real space. The envelope of the group of these spheres draws the target shape. This process is formulated as follows. We express the group of the spheres as $F_{\mathrm{C}}(x, y, z; X, Y, Z) = 0$, where we define

$$F_{\mathrm{C}}(x, y, z; X, Y, Z) = (x - X)^2 + (y - Y)^2 + z^2 - Z^2. \tag{5}$$

The envelope of this group of the spheres satisfies

$$F_{\mathrm{C}}(x, y, z; X, Y, Z) = 0, \tag{6}$$

$$\partial F_{\mathrm{C}}(x, y, z; X, Y, Z)/\partial X = 0, \tag{7}$$

$$\partial F_{\mathrm{C}}(x, y, z; X, Y, Z)/\partial Y = 0. \tag{8}$$

Here, the partial derivative means the derivative that is independent of all variables except for Z. Here, we note that Z is uniquely determined by X and Y. We solve these conditions for x, y and z and obtain

$$\begin{cases} x &= X - Z\partial Z/\partial X \\ y &= Y - Z\partial Z/\partial Y \\ z &= Z\sqrt{1-(\partial Z/\partial X)^2-(\partial Z/\partial Y)^2}. \end{cases} \tag{9}$$

We call the transform of Eq. (9) 3-D IBST (3-dimensional Inverse Boundary Scattering Transform) or simply, just IBST [33]. This transform is the inverse transform of the 3-D BST in Eq. (3), which we prove in the section that follows. The existence of the inverse transform is meaningful because it can be used for the direct and unique estimation of target shapes. The estimated target boundaries are expressed not as an image but as surfaces. This is both the advantage and the characteristic of our algorithm.

Additionally, the condition

$$(\partial Z/\partial X)^2 + (\partial Z/\partial Y)^2 \le 1, \tag{10}$$

should be satisfied because this inequality guarantees z in Eq. (9) to be a real number. The equal sign in Eq. (10) holds if the target object is on x-y plane.

3.3 Proof of the Reversibility of BST

We replace x, y, z by x_0, y_0, z_0 in Eq. (9) to distinguish them from the original target shape x, y, z as

$$x_0 = X - Z\partial Z/\partial X \tag{11}$$

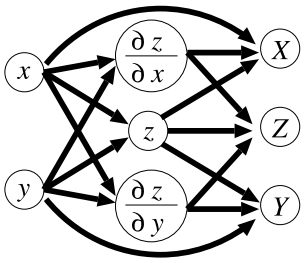

Fig. 3 Chain rule applied to BST.

$$y_0 = Y - Z\partial Z/\partial Y \tag{12}$$

$$z_0 = Z\sqrt{1-(\partial Z/\partial X)^2-(\partial Z/\partial Y)^2}. \tag{13}$$

Our objective is to prove the proposition that $x = x_0$, $y = y_0$ and $z = z_0$ hold, which means that the inverse transform of Eq. (3) is expressed as Eq. (9).

First, to prove this hypothesis we derive $\partial Z/\partial X$ and $\partial Z/\partial Y$. Figure 3 shows the dependency of the variables in BST, in which Z is determined by $z, \partial z/\partial x$ and $\partial z/\partial y$, and all of them are determined by x and y, which have 2 degrees of freedom. We assume Y is constant because $\partial Z/\partial X$ means the partial derivative with constant Y, which reduces the degrees of freedom to 1. For a fixed Y, y depends on x for example. The physical meaning of this dependency follows. If we scan an antenna in the X-direction for a fixed Y, the locus of the scattering center (x, y, z) becomes a curved line, where x and y are not independent of each other. Therefore, we can calculate the derivative $\mathrm{d}y/\mathrm{d}x$ for the fixed Y. First, we differentiate X in Eq. (3) for x in terms of an ordinary derivative and solve for $\mathrm{d}(zz_x)/\mathrm{d}x|_{Y=\text{const.}}$ as

$$\mathrm{d}(zz_x)/\mathrm{d}x|_{Y=\text{const.}} = \mathrm{d}X/\mathrm{d}x|_{Y=\text{const.}} - 1, \tag{14}$$

where z_x denotes $\partial z/\partial x$ for example. Similarly, we differentiate Y in Eq. (3) for x and obtain

$$\mathrm{d}(zz_y)/\mathrm{d}x|_{Y=\text{const.}} = -\mathrm{d}y/\mathrm{d}x|_{Y=\text{const.}}. \tag{15}$$

Hereafter, for simplicity we sometimes omit the suffix $Y = \text{const.}$. Next, we differentiate Z in Eq. (3) for x as

$$\frac{\mathrm{d}Z}{\mathrm{d}x} = \left\{ z\frac{\mathrm{d}z}{\mathrm{d}x} + zz_x\frac{\mathrm{d}(zz_x)}{\mathrm{d}x} + zz_y\frac{\mathrm{d}(zz_y)}{\mathrm{d}x} \right\}/Z. \tag{16}$$

Substituting Eqs. (14) and (15) to Eq. (16), we obtain

$$\frac{\mathrm{d}Z}{\mathrm{d}x} = \left\{ zz_x\left(\frac{\mathrm{d}X}{\mathrm{d}x} - 1\right) + z\left(\frac{\mathrm{d}z}{\mathrm{d}x} - z_y\frac{\mathrm{d}y}{\mathrm{d}x}\right) \right\}/Z. \tag{17}$$

Here, $\mathrm{d}z/\mathrm{d}x|_{Y=\text{const.}} = z_x + z_y\mathrm{d}y/\mathrm{d}x|_{Y=\text{const.}}$ holds because of the chain rule. Therefore, Eq. (17) can be simplified as

$$\mathrm{d}Z/\mathrm{d}x = z_x\frac{\mathrm{d}X}{\mathrm{d}x}/\sqrt{1+z_x^2+z_y^2}. \tag{18}$$

Finally, we obtain

$$\partial Z/\partial X = \mathrm{d}Z/\mathrm{d}X|_{Y=\text{const.}} \tag{19}$$

$$= z_x/\sqrt{1+z_x^2+z_y^2}. \tag{20}$$

Similarly, dZ/dY is also derived as

$$\partial Z/\partial Y = z_y/\sqrt{1+z_x^2+z_y^2}. \quad (21)$$

Next, we substitute Eq. (20), X and Z of Eq. (3) to Eq. (11) and obtain $x_0 = x$. Similarly, we substitute Eq. (21), Y and Z of Eq. (3) to Eq. (12) and obtain $y_0 = y$. Finally, we substitute Eqs. (20), (21) and Z of Eq. (3) to Eq. (13) and obtain $z_0 = z$. Now, we have proved that the 3-D BST in Eq. (3) is a reversible transform, and its inverse transform is given as Eq. (9).

4. Proposed Algorithm

In this section, we propose a 3-dimensional imaging algorithm, the 3-D SEABED algorithm, which is based on the 3-D IBST described above. Figure 4 illustrates the outline of the algorithm we propose in this paper. First, we apply a filter to the received signal; where this filter is matched to the transmitted waveform. Next, we extract quasi wavefronts from the received signals. We detect points (X, Y, Z) that satisfy

$$\partial s(X, Y, Z)/\partial Z = 0, \quad (22)$$

and

$$|s(X, Y, Z)| \geq T_s, \quad (23)$$

where T_s is a threshold to prevent noise values being picked up. We express the detected points as $(X_i, Y_j, Z_{i,j,k})$ $(i = 1, \cdots, I, j = 1, \cdots, J, k = 1, \cdots, K)$, where K is the maximum number of points detected for each antenna position. Here, note that X_i and Y_i are discrete values with the spatial interval d of the measurement.

Next, we sequentially connect these points and obtain quasi wavefronts, which are single valued functions. As described in the previous section, any quasi wavefronts have to satisfy the condition in Eq. (10) as

$$(\partial Z/\partial X)^2 + (\partial Z/\partial Y)^2 = \left|\mathrm{grad}Z\right|^2 \leq 1. \quad (24)$$

We deal with four antenna positions on vertexes of a square as a unit as

$$Q_{i,j} = \{(X_i, Y_j), (X_{i+1}, Y_j), (X_i, Y_{j+1}), (X_{i+1}, Y_{j+1})\}. \quad (25)$$

The approximate gradient at the center of this square $Q_{i,j}$ is easily calculated as

$$\begin{bmatrix} \frac{\partial Z}{\partial X} \\ \frac{\partial Z}{\partial Y} \end{bmatrix} \simeq \begin{bmatrix} \frac{Z_{i+1,j}+Z_{i+1,j+1}-Z_{i,j}-Z_{i,j+1}}{2(X_{i+1}-X_i)} \\ \frac{Z_{i,j+1}+Z_{i+1,j+1}-Z_{i,j}-Z_{i+1,j}}{2(Y_{j+1}-Y_j)} \end{bmatrix}, \quad (26)$$

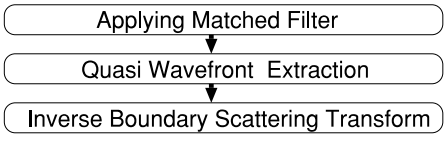

Fig. 4 Outline of the proposed algorithm.

where k, the index of Z is omitted for simplicity. Therefore, the condition of Eq. (24) is approximately checked for each square $Q_{i,j}$. We define P as the set of all squares $Q_{i,j}$ $(i, j = 1, 2, \cdots)$ with all the antennas used. Figure 5 illustrates the defined squares $Q_{i,j}$ and antenna positions. We define R as the domain of the quasi wavefront, which is updated in the following procedures. Figure 6 shows the relationship between the set P, the squares $Q_{i,j}$, the domain R and the quasi-wavefront. We estimate quasi wavefronts with a token that goes around the boundary of R, and checks whether there is another candidate square to include into R with the condition of Eq. (24). The extraction algorithm of quasi wavefronts is as follows:

1. The first square Q is arbitrarily selected only if it satisfies the condition of Eq. (24). The estimated domain of a quasi wavefront R is now equivalent to Q now. We set a token on one of the four sides of Q, and go to step 2.
2. The token checks the gradient condition for the square outside R with one or a few sides in common with R for each k. Then, the token goes counterclockwise to the next side of R. If the checked square is not in P, go to step 4. If the gradient condition is satisfied for a certain k, go to step 3. Otherwise, go to step 4.
3. The domain of the quasi wavefront R is updated by adding the new square, and go to step 2.
4. If the token has finished the round trip without finding any new squares outside, go to step 5. Otherwise, go to step 2.

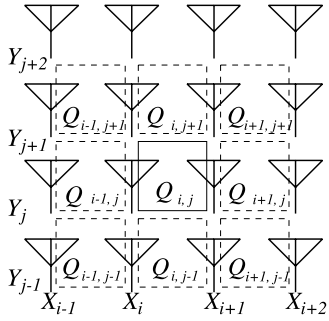

Fig. 5 Defined squares for antenna positions.

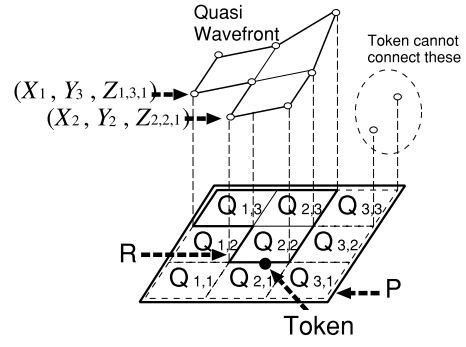

Fig. 6 Relationship between the quasi-wavefront, the set P, the squares $Q_{i,j}$ and the domain R.

5. The procedure is finished with the final quasi wavefront and its domain R.

This procedure is repeated for each initial square Q, and we obtain multiple quasi wavefronts. The duplicated quasi wavefronts are detected and eliminated. Steps 2 and 3 above require careful treatment because there are some cases that depend on the boundary shape of R. Figure 7 shows an example of the square expansion processes, where the black circle is the position of the token, and the set of the squares is the already estimated quasi wavefront domain R. At the 1st step in this figure, a token checked the gradient condition. Next, R is updated by adding 2 points in the 2nd step, where the gray square is the new one that is added. Note that one square is composed of 4 points as in Eq. (25). Therefore, two vertexes were already in the previous R, and the other two vertexes join R in the 2nd step. At the 3rd step, R is updated by adding 1 point because the new square has 2 sides in common with R. At the 5th step, R is updated without adding any new points.

Additionally, if the antenna positions of the new square already belong to R, we do not update the boundary of R although we update the quasi wavefront and R as in Fig. 8. This exceptional definition of the boundary is needed to avoid making a hole in R, otherwise the token cannot get to another area.

In this way, quasi wavefronts are extracted. Next, we calculate $\partial Z/\partial X$ and $\partial Z/\partial Y$ for the extracted quasi wavefront. Finally, we apply IBST in Eq. (9) to the data and obtain an estimated target surface.

We propose the procedure described above to extract the quasi-wavefronts. If we simply connect all the points (X, Y, Z) which satisfy the condition in Eq. (24), a serious trouble occurs as follows. First, the simple procedure can mistakingly connect the two points which are not connected with our algorithm in Fig. 6. Although these two points are close to each other, we cannot calculate the partial derivative for $Q_{3,3}$ because four points are required as in Eq. (26). Therefore, some of the connected points have the partial derivatives, and the others do not, which is too confusing to apply the IBST to the quasi-wavefront. In order to avoid this difficulty, we organizationally expand the quasi-wavefront with our proposed algorithm.

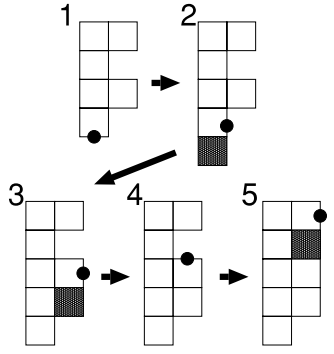

Fig. 7 Example of the quasi wavefront extraction procedure.

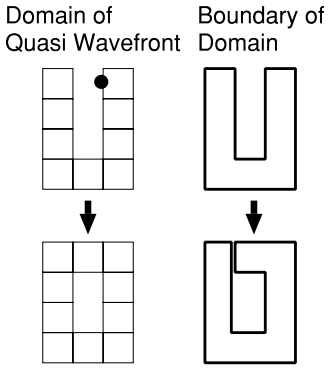

Fig. 8 Exceptional boundary definition of the domain.

5. Application Example

5.1 Imaging by Numerical Simulation

We present an example application of the proposed algorithm. The assumed target is shown in Fig. 9. The inner part of the surface is filled with a perfect electric conductor. The scanning plane is $z = 3$, which means that the plane is 1λ apart from the nearest target surface. We obtain the received data $s(X, Y, Z)$ using the FDTD method, and assume $S/N = \infty$. First, we apply a filter matched for the transmitted waveform. For simplicity, we show part of the observed signals for $X = 0$ in Fig. 10. Next, we estimate the candidate points $X_i, Y_j, Z_{i,j,k}$ based on the conditions in Eqs. (22) and (23) where we empirically set $T_s = S_0/10$ with the maximum peak S_0 of the received signal. We set $K = 1$ for simplicity. Figure 11 shows part of the candidate points for $X = 0$. Then, we connect these points by expanding the domain of the quasi wavefront, and obtain a quasi wavefront

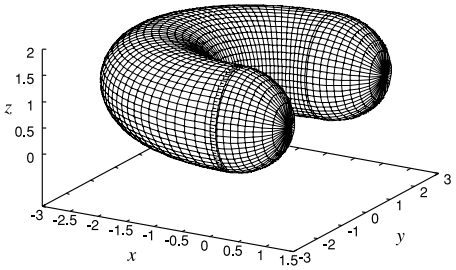

Fig. 9 True target shape.

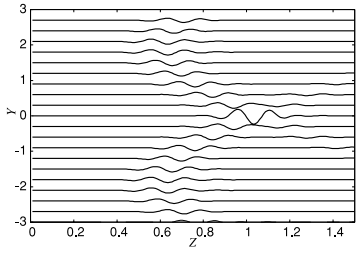

Fig. 10 Observed signals for $X = 0$.

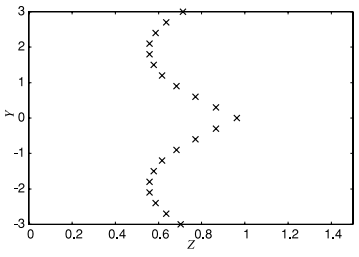

Fig. 11 Estimated candidate points for $X = 0$.

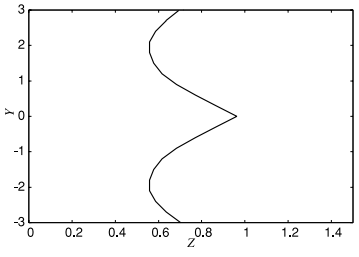

Fig. 12 Estimated quasi wavefront for $X = 0$.

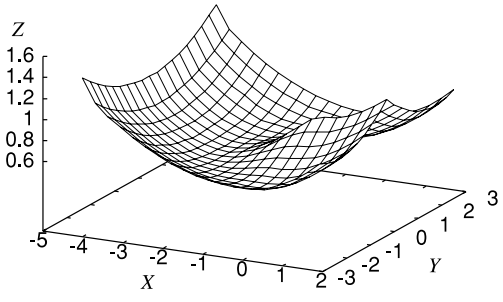

Fig. 13 Extracted quasi wavefront.

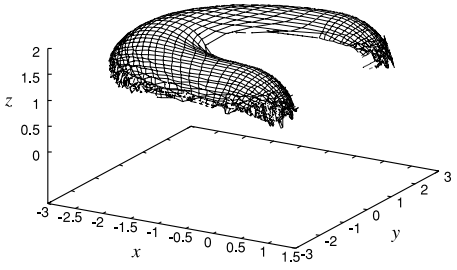

Fig. 14 Estimated target shape. Computation time for the reconstruction is 0.1 sec.

from $s(X, Y, Z)$. Figure 12 shows part of the quasi wavefront for $X = 0$. In reality, a quasi wavefront is extracted for all X and Y as in Fig. 13. We calculate $\partial Z/\partial X$ and $\partial Z/\partial Y$ and apply IBST to the quasi wavefront. Finally, we obtain the estimated target shape as in Fig. 14 for the data acquisition at 51×51 positions with intervals of $\lambda/4$. As for the calculation time, the proposed algorithm in this case takes 0.1 sec with a single Xeon 2.8 GHz processor.

Figure 15 shows the difference between the estimated image and the true image. The broken line in this figure is the cross section outline of the target shape. The av-

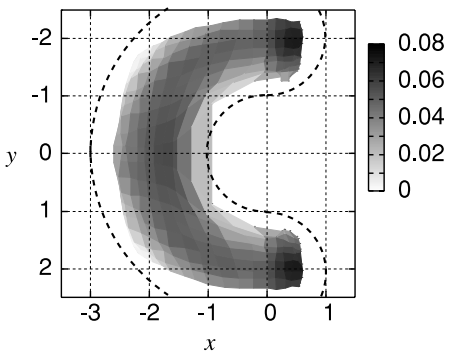

Fig. 15 Estimation error for the SEABED algorithm.

eraged error is 4.4×10^{-2} wavelength for the Z direction. The error is large in the region where the antenna is close to the target because the received signals are influenced by the near field. Additionally, the estimation error is particularly large at the two ends of the target shape around $(0.5, 2)$ and $(0.5, -2)$, which is also caused by the waveform distortion. The ends of the target have comparatively large curvatures and emphasize the diffraction effect, which leads to the waveform distortion. This systematic error is caused by the applied matched filter that is matched for the transmitted waveform, not for the received waveform. For 2-D imaging by SEABED, estimation accuracy can be improved by iteratively estimating the received waveforms using the target shape estimated in the previous step [34]. An important future task will be to apply the waveform estimation technique to the 3-D SEABED algorithm.

In this paper, we investigate our proposed algorithm with ideal data without noise. However, it is important to study the imaging performance of the proposed algorithm with realistic data, which will have noise. The references [35], [36] dealt with stabilization techniques for the SEABED algorithm to improve the performance for noisy data obtained experimentally.

The SEABED algorithm also works for targets far from the antenna, although we have assumed that the target is relatively close to the antenna in the simulation. We explain some differences between the near and far target locations from the antenna. First, the scattered waveform from the near targets is distorted by the near-field effect, which leads to the estimation error described above. Second, we need a large scanning area to obtain the entire image for a target far from the antenna. This is because the SEABED algorithm utilizes the scattered waves whose incidence direction is perpendicular to the target surface. Third, the sensitivity of the algorithm to noise become large for the targets far from the antenna. The sensitivity to noise can be analyzed with the total derivatives of Eq. (9) as

$$\mathrm{d}x = \frac{\partial x}{\partial Z}\mathrm{d}Z + \frac{\partial x}{\partial Z_X}\mathrm{d}Z_X, \tag{27}$$

$$= -Z_X\mathrm{d}Z - Z\mathrm{d}Z_X, \tag{28}$$

$$\mathrm{d}z = \frac{\partial z}{\partial Z}\mathrm{d}Z + \frac{\partial z}{\partial Z_X}\mathrm{d}Z_X + \frac{\partial z}{\partial Z_Y}\mathrm{d}Z_Y, \tag{29}$$

$$= \xi \mathrm{d}Z - \frac{ZZ_X}{\xi}\mathrm{d}Z_X - \frac{ZZ_Y}{\xi}\mathrm{d}Z_Y, \tag{30}$$

where we define $\xi = \sqrt{1 - Z_X^2 - Z_Y^2}$ for simplicity. Here we omit dy because it is similar to dx. These equations include Z in the sensitivity to dZ_X for dx, and dZ_X and dZ_Y for dz. Note that these sensitivities are dominant for the total estimation error because the derivative operations emphasize the random component. Therefore, the estimation error caused by the noise and the timing jitters become large as the target gets far from the antenna if the observation intervals $\Delta X = X_{i+1} - X_i$ and $\Delta Y = Y_{j+1} - Y_j$ are fixed. However, these intervals naturally become large because we have to set the large scanning area for the far target. Consequently, the deterioration of estimation accuracy for large Z is moderate in a practical situation.

5.2 Comparison with a Conventional Algorithm

We compare the proposed SEABED method with a conventional imaging algorithm, the synthetic aperture method. The synthetic aperture method is often used for targets far from the antenna because 1-dimensional synthetic aperture processing, which is independent of the pulse compression for the range direction, can be utilized. However, it is difficult to apply this 1-dimensional synthetic aperture processing for nearby targets. Instead, the image $S(x, y, z)$ is obtained from the data $s(X, Y, Z)$ as

$$S(x,y,z) = \int s\left(X, Y, \sqrt{(X-x)^2 + (Y-y)^2 + z^2}\right) \mathrm{d}X\mathrm{d}Y. \tag{31}$$

We calculate this integral only if the signal satisfies $|s(X, Y, Z)| > T_\mathrm{s}$, where we set the same threshold T_s as in Eq. (23) for the SEABED algorithm. The setting of the threshold reduces the computational time, which enables us to fairly compare the performances of the SEABED algorithm and the synthetic aperture processing. Further, to make it easy to compare the proposed algorithm and the synthetic aperture method, we also define the surface $S_0(x, y)$ as

$$S_0(x, y) = \arg\max_z |S(x, y, z)|, \tag{32}$$

which is the estimated surface of the target. Here, we assume the same target shape dealt with in the previous section. We calculate $S(x, y, z)$ with $90 \times 90 \times 90$ grids with the empirically chosen intervals $\Delta x = 0.15\lambda$, $\Delta y = 0.19\lambda$ and $\Delta z = 0.015\lambda$, and then obtain the surface $S_0(x, y)$.

Figures 16 and 17 shows the estimated target shape using the SEABED algorithm and the estimated target shape $S_0(x, y)$ using the synthetic aperture method, respectively. The image obtained by the synthetic aperture method contains undesired interference images. On the other hand, the proposed SEABED algorithm does not contain these, because the interference components have been eliminated in the step for the extraction of the quasi wavefronts. We see that the SEABED algorithm can obtain the image even around the edges where the synthetic aperture processing

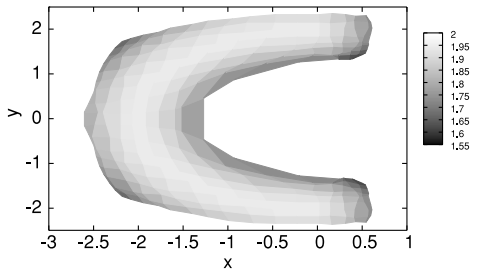

Fig. 16 Estimated target shape using the SEABED algorithm (0.1 sec).

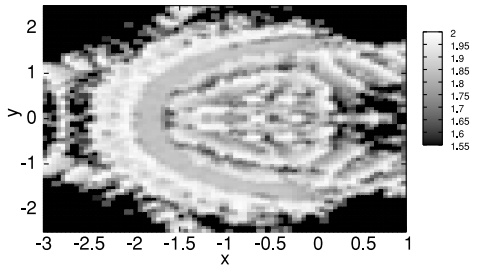

Fig. 17 Estimated target shape using synthetic aperture processing (18 min).

Table 1 Computation of the synthetic aperture and the SEABED for each signal.

	Synthetic Aperture	SEABED
Addition	3,645,000	6
Multiplication	2,187,000	5
Division	0	2
Squre root	729,000	1

cannot. The reason is following. The synthetic aperture processing directly utilizes the signal intensity to obtain the image, while the SEABED algorithm does not. The image $S(x, y, z)$ with the synthetic aperture processing has small values around the target edges because the signal power is small there. Because this small value in the image is masked by undesired interference images, the target edges cannot be estimated by the synthetic aperture processing. On the other hand, the SEABED algorithm utilizes the delay time of continuously connected peaks instead of the signal intensity itself. This process prevents the deterioration of the obtained image although this technique works only for the targets with clear boundaries.

The calculation time for the synthetic aperture method is about 18 minutes with a single Xeon 2.8 GHz processor. On the other hand, the proposed algorithm can obtain the entire image within 0.1 sec, which is remarkably fast compared to the synthetic aperture method. Table 1 shows the comparison of the computations for the synthetic aperture processing and the SEABED algorithm. The number in each column is the number of computations for each antenna position (X, Y). For simplicity, we only consider Eqs. (9) and (31) without other factors including the effect of the thresholds and the extraction of quasi-wavefronts. The synthetic aperture processing requires to perform the summation in

Eq. (31) for $90 \times 90 \times 90$ times, which is the number of grids that we assumed in this paper. On the other hand, the computation of the SEABED algorithm is remarkably reduced because the SEABED algorithm does not utilize the grid model.

6. Conclusions

In this paper, we have proposed a new 3-dimensional imaging algorithm based on BST for pulse radar systems. BST is known as a reversible transform between target surfaces and the received wave delay for 2-dimensional systems. We have extended BST to 3-dimensional systems and apply it for 3-dimensional imaging. First, we have shown the extended transform and its inverse transform. Second, we have proposed a 3-dimensional imaging algorithm based on BST. Finally, we have presented an example application of the proposed algorithm. We have clarified that the proposed algorithm's calculation time is considerably shorter than conventional algorithms, so that the proposed algorithm can be readily implemented to real-time applications. Additionally, the estimated target shape is accurate enough under the condition that a directly scattered waveform can be obtained. In this paper, we have shown an example application without noise. Investigating the performance of the proposed algorithm under noisy conditions will be an important future task.

Acknowledgment

We thank Prof. Toru Sato at The Department of Communications and Computer Engineering, Graduate School of Informatics, Kyoto University, Japan for his valuable advice.

References

[1] J.P. Fitch, Synthetic Aperture Radar, Springer-Verlag, New York, 1988.
[2] T. Suzuki and I. Arai, "Advance on underground radars," IEICE Trans. Commun., vol.E74-B, no.2, pp.289–294, Feb. 1991.
[3] E.J. Bond, X. Li, S.C. Hagness, and B.D. van Veen, "Microwave imaging via space-time beamforming for early detection of breast cancer," IEEE Trans. Antennas Propag., vol.51, no.8, pp.1690–1705, 2003.
[4] R.M. Narayanan, X. Xu, and J.A. Henning, "Radar penetration imaging using ultra-wideband (UWB) random noise waveforms," IEE Proc.-Radar Sonar Navig., vol.151, no.3, pp.143–148, 2004.
[5] J. van der Kruk, C.P.A. Wapenaar, J.T. Fokkema, and P.M. van den Berg, "Three-dimensional imaging of multicomponent ground-penetrating radar data," Geophysics, vol.68, no.4, pp.1241–1254, 2003.
[6] M.B. Dobrin and C.H. Savit, Introduction to Geophysical Prospecting, Fourth Edition, McGraw-hill, 1988.
[7] C.J. Leuschen and R.G. Plumb, "A matched-filter-based reverse-time migration algorithm for grond-penetrating radar data," IEEE Trans. Geosci. Remote Sens., vol.39, no.5, pp.929–936, May 2001.
[8] J.V. Candy and C. Pichot, "Active microwave imaging: A model-based approach," IEEE Trans. Antennas Propag., vol.39, no.3, pp.285–290, 1991.
[9] G.P. Otto and W.C. Chew, "Microwave inverse scattering—Local shape function imaging for improved resolution of strong scatterers," IEEE Trans. Microw. Theory Tech., vol.42, no.1, pp.137–142, 1994.
[10] I.T. Rekanos, T.V. Yioultsis, and T.D. Tsiboukis, "Inverse scattering using the finite-element method and a nonlinear optimization technique," IEEE Trans. Microw. Theory Tech., vol.47, no.3, pp.336–344, 1999.
[11] C.C. Chiu and W.T. Chen, "Electromagnetic imaging for an imperfectly conducting cylinder by the genetic algorithm," IEEE Trans. Microw. Theory Tech., vol.48, no.11, pp.1901–1905, 2000.
[12] C. Chiu, C. Li, and W. Chan, "Image reconstruction of a buried conductor by the genetic algorithm," IEICE Trans. Electron., vol.E84-C, no.12, pp.1946–1951, Dec. 2001.
[13] T. Takenaka, H. Jia, and T. Tanaka, "Microwave imaging of an anisotropic cylindrical object by a forward-backward time-stepping method," IEICE Trans. Electron., vol.E84-C, no.12, pp.1910–1916, Dec. 2001.
[14] R. Ferraye, J.-Y. Dauvignac, and C. Pichot, "An inverse scattering method based on contour deformations by meas of a level set method using frequency hoping technique," IEEE Trans. Antennas Propag., vol.51, no.5, pp.1100–1113, 2003.
[15] T. Sato, K. Takeda, T. Nagamatsu, T. Wakayama, I. Kimura, and T. Shinbo, "Automatic signal processing of front monitor radar for tunnelling machines," IEEE Trans. Geosci. Remote Sens., vol.35, no.2, pp.354–359, 1997.
[16] T. Sato, T. Wakayama, and K. Takemura, "An imaging algorithm of objects embedded in a lossy dispersive medium for subsurface radar data processing," IEEE Trans. Geosci. Remote Sens., vol.38, no.1, pp.296–303, 2000.
[17] A. Franchois and C. Pichot, "Microwave imaging—Complex permittivity reconstruction with a Levenberg-Marquardt method," IEEE Trans. Antennas Propag., vol.45, no.2, pp.203–215, 1997.
[18] C. Zhou and L. Liu, "Radar-diffraction tomography using the modified quasi-linear approximation," IEEE Trans. Geosci. Remote Sens., vol.38, no.1, pp.404–415, 2000.
[19] A. Abubakar, P.M. Berg, and B.J. Kooij, "A conjugate gradient contrast source technique for 3D profile inversion," IEICE Trans. Electron., vol.E83-C, no.12, pp.1864–1874, Dec. 2000.
[20] N.V. Budko, R.F. Remis, and P.M. Berg, "Two-dimensional imaging and effective inversion of a three-dimensional buried object," IEICE Trans. Electron., vol.E83-C, no.12, pp.1889–1895, Dec. 2000.
[21] C. Dourthe, C. Pichot, J.Y. Dauvignac, L. Blanc-feraud, and M. Barlaud, "Regularized bi-conjugate gradient algorithm for tomographic reconstruction of buried objects," IEICE Trans. Electron., vol.E83-C, no.12, pp.1858–1863, Dec. 2000.
[22] Y. Yu, T. Yu, and L. Carin, "Three-dimensional inverse scattering of a dielectric target embedded in a lossy half-space," IEEE Trans. Geosci. Remote Sens., vol.42, no.5, pp.957–973, 2004.
[23] T.J. Cui, Y. Qin, G.L. Wang, and W.C. Chew, "High-order inversion formulas for low-frequency imaging of 2D buried targets," Proc. 2004 IEEE Antennas and Propagation Society International Symposium, vol.1, pp.189–192, 2004.
[24] D. Nahamoo, S.X. Pan, and A.C. Kak, "Synthetic aparture diffraction tomography and its interpolation-free computer implementation," IEEE Trans. Sonics Ultrason., vol.31, no.4, pp.218–229, 1984.
[25] C. Pichot, L. Jofre, G. Peronnet, and J.C. Bolomey, "Active microwave imaging of inhomogeneous bodies," IEEE Trans. Antennas Propag., vol.33, no.4, pp.416–425, 1985.
[26] T.B. Hansen and P.M. Johansen, "Inversion scheme for monostatic ground penetrating radar that takes into account the planar air-soil interface," IEEE Trans. Geosci. Remote Sens., vol.38, no.1, pp.496–506, Jan. 2000.
[27] T.J. Cui and W.C. Chew, "Diffraction tomographic algorithm for the detection of three-dimensional objects buried in a lossy half space," IEEE Trans. Antennas Propag., vol.50, no.1, pp.42–49, Jan. 2002.
[28] T.J. Cui, W.C. Chew, X.X. Yin, and W. Hong, "Study of resolution and super resolution in electromagnetic imaging for half-space problems," IEEE Trans. Antennas Propag., vol.52, no.6, pp.1398–1411, 2004.

[29] T. Sakamoto and T. Sato, "A target shape estimation algorithm for pulse radar systems based on boundary scattering transform," IEICE Trans. Commun., vol.E87-B, no.5, pp.1357–1365, May 2004.
[30] T. Sakamoto and T. Sato, "Fast imaging of a target in inhomogeneous media for pulse radar systems," Proc. 2004 IEEE International Geoscience and Remote Sensing Symposium, vol.3, pp.2070–2073, Sept. 2004.
[31] T. Sakamoto and T. Sato, "A phase compensation algorithm for high-resolution pulse radar systems," IEICE Trans. Commun., vol.E87-B, no.11, pp.3314–3321, Nov. 2004.
[32] T. Sakamoto and T. Sato, "A phase compensation algorithm for high-resolution pulse radar systems," Proc. 2004 International Symposium on Antennas and Propagation, pp.585–588, Aug. 2004.
[33] T. Sakamoto and T. Sato, "A fast algorithm of 3-dimensional imaging for pulse radar systems," Proc. 2004 IEEE AP-S International Symposium and USNC/URSI National Radio Science Meeting, vol.2, pp.2099–2102, June 2004.
[34] S. Kidera, T. Sakamoto, and T. Sato, "A high-resolution imaging algorithm based on scattered waveform estimation for UWB pulse radar systems," Proc. 2005 IEEE International Geoscience and Remote Sensing Symposium, pp.1725–1728, July 2005.
[35] T. Sakamoto, S. Kidera, T. Sato, T. Mitani, and S. Sugino, "An experimental study on a fast imaging algorithm for UWB pulse radar systems," Proc. 2005 IEEE AP-S International Symposium and USNC/URSI National Radio Science Meeting, P24.5, July 2005.
[36] T. Sakamoto, S. Kidera, T. Sato, T. Mitani, and S. Sugino, "An experimental study on a fast and accurate 3-D imaging algorithm for UWB pulse radar systems," 28th General Assembly of International Union of Radio Science (URSI), F05.7, Oct. 2005.

Takuya Sakamoto was born in Nara, Japan in 1977. Dr. Sakamoto received his B.E. degree from Kyoto University in 2000, and M.I. and Ph.D. degrees from the Graduate School of Informatics, Kyoto University in 2002 and 2005, respectively. He is a research associate in the Department of Communications and Computer Engineering, Graduate School of Informatics, Kyoto University. His current research interest is in digital signal processing. He is a member of the IEEJ and the IEEE.